Multi-harmonic Imaging in the Second Near-Infrared Window of Nanoparticle-Labeled Stem Cells as a Monitoring Tool in Tissue Depth

Laurence Dubreil,[†] Isabelle Leroux,[†] Mireille Ledevin,[†] Cindy Schleder,[†] Lydie Lagalice,[†] Claire Lovo,[†] Romain Fleurisson,[†] Solene Passemard,[‡] Vasyl Kilin,[§] Sandrine Gerber-Lemaire,[‡] Marie-Anne Colle,[†] Luigi Bonacina,*[§] and Karl Rouger[†]

[†]PAnTher, INRA, École nationale vétérinaire, agro-alimentaire et de l'alimentation Nantes-Atlantique (Oniris), Université Bretagne Loire (UBL), Nantes F-44307, France
[‡]Group for Functionalized Biomaterials, École Polytechnique Fédérale de Lausanne, Station 6, 1015 Lausanne, Switzerland
[§]GAP-Biophotonics, Université de Genève, 22 chemin de Pinchat, 1211 Genève 4, Switzerland

ABSTRACT: In order to assess the therapeutic potential of cell-based strategies, it is of paramount importance to elaborate and validate tools for monitoring the behavior of injected cells in terms of tissue dissemination and engraftment properties. Here, we apply bismuth ferrite harmonic nanoparticles (BFO HNPs) to *in vitro* expanded human skeletal muscle-derived stem cells (hMuStem cells), an attractive therapeutic avenue for patients suffering from Duchenne muscular dystrophy (DMD). We demonstrate the possibility of stem cell labeling with HNPs. We also show that the simultaneous acquisition of second- and third-harmonic generation (SHG and THG) from BFO HNPs helps separate their response from tissue background, with a net increase in imaging selectivity, which could be particularly important in pathologic context that is defined by a highly remodelling tissue. We demonstrate the possibility of identifying <100 nm HNPs in depth of muscle tissue at more than 1 mm from the surface, taking full advantage of the extended imaging penetration depth allowed by multiphoton microscopy in the second near-infrared window (NIR-II). Based on this successful assessment, we monitor over 14 days any modification on proliferation and morphology features of hMuStem cells upon exposure to PEG-coated BFO HNPs at different concentrations, revealing their high biocompatibility. Successively, we succeed in detecting individual HNP-labeled hMuStem cells in skeletal muscle tissue after their intramuscular injection.

KEYWORDS: Duchenne muscular dystrophy, cell therapy, harmonic nanoparticles, second-harmonic generation, third-harmonic generation, second near-infrared window
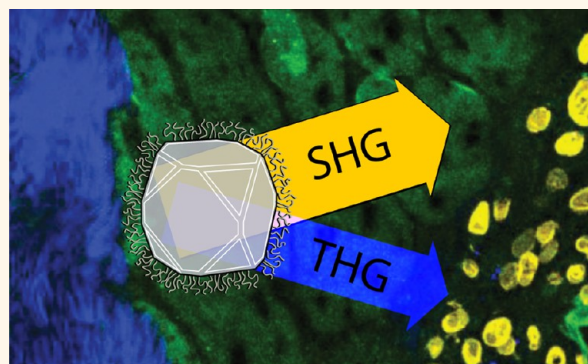
D uchenne muscular dystrophy (DMD) is a fatal X-linked recessive muscle disease that represents the most common form of muscular dystrophy, affecting about one in 3500 to 5500 male births.[1,2] It is caused by mutations or deletions in the gene encoding dystrophin, leading to the lack of dystrophin protein. This results in muscle fiber degeneration followed by severe endomysial sclerosis, leading to progressive muscle weakness and premature death at the age of 20–30 years. Currently, there is no effective treatment for DMD. Over the last years, we showed that a stem cell population (named MuStem cells) isolated from healthy dog skeletal muscle induces long-term muscle repair and striking clinical efficacy after its systemic delivery in the dystrophic dog,

representing the clinically relevant DMD animal model.[3−6] More recently, we isolated the human counterparts (hMuStem cells) and demonstrated that they share the same phenotypic and *in vitro* behavioral features of canine cells.[7,8] In a clinical prospect, to position this cell population as a potential therapeutic product, several burning questions must be duly addressed, including the biodistribution of the cell agent delivered locally and/or systemically. This is of utmost

importance as it results from the main notions of safety and efficiency of the proposed strategies. A possible approach is labeling hMuStem cells by nanoparticles prior to the transplantation protocol. Nanoparticles in fact can provide contrast for one or more detection techniques and allow tracking cells' position and monitoring their distribution over time.[9,10] However, among all existing techniques (magnetic resonance imaging, computed tomography, positron emission tomography, ultrasound, *etc.*), only optical ones provide the spatial resolution necessary for individual cell tracking.[11] On the negative side, optical approaches inherently possess limited penetration depth and often offer poor selectivity when the structures of interest are embedded in strongly autofluorescent and scattering tissues. To address these shortcomings, in recent years, several authors have highlighted the advantages of using the so-called second near-infrared window (NIR-II, 1−1.4 μm)[12] also in connection with nanotechnology-based approaches.[13] By a clever choice of the excitation wavelength, tissue autofluorescence can be eliminated, absorption by water can be locally minimized, and scattering can be severely reduced with respect to NIR-I (600−800 nm).

In this work, we use bismuth ferrite (BiFeO$_3$, BFO) harmonic nanoparticles (HNPs) to label hMuStem cells. The choice of this nanomaterial is motivated by the necessity to maximize imaging depth and to maintain high selectivity against endogenous tissue emission. HNPs have a net advantage with respect to other optically active nanoparticles because they present no constrain for the excitation wavelength and can be efficiently employed as NIR-II probes (and even in the further infrared windows)[12] differently from most of the optical particles that have visible or UV−visible bands.[14] Concerning imaging selectivity, we have recently shown how the simple colocalization of simultaneously emitted SHG and THG by HNPs can be used as robust criterion to identify HNPs in optically congested environments with minimal hindrance by autofluorescence or endogenous SHG and THG[15] from collagen and adipose tissue, respectively.[16,17] Among metal-oxide HNPs, BFO is the first material of choice, as its nonlinear coefficients are the highest,[18,19] and the intensity ratio between the two nonlinear emissions is conveniently low (SHG/THG = 30) when excited in NIR-II at 1300 nm under typical imaging conditions.[15,20] On top of these appealing characteristics, HNPs are inherently not bleaching/blinking nor saturating due to their excitation mechanism involving exclusively virtual electronic states.[14] Recently, we have provided an assessment of the effects of *in vitro* exposure of human lines (adenocarcinoma, lung squamous carcinoma, and acute monocytic leukemia) to uncoated and PEG [poly(ethylene glycol)]-coated BFO HNPs in the form of cytotoxicity, hemolytic response, and biocompatibility. Our results demonstrated the high biocompatibility of these particles for these human cell lines.[21]

In the following, we first perform stem cell labeling with HNPs to determine our ability to select a cell track tool, and in a second time, we perform an assessment focused on the optical properties of HNPs interacting with the relevant biological systems investigated in this work, namely, muscle tissue. In particular, we investigate the depth at which isolated HNPs can be retrieved in tissue not submitted to any pretreatment. Successively, we define the optimal conditions for labeling hMuStem cells with BFO HNPs and determine their biocompatibility by quantifying cells' survival rate and proliferation behavior over 14 days. Finally, we demonstrate

the possibility to detect labeled stem cells injected in muscles with high contrast against endogenous and exogenous tissue background.

RESULTS

BFO HNP Imaging Properties. This first section highlights the advantages of the NIR-II HNP approach in the context of cell tracking in tissues. In Figure 1, we present the images of *in*
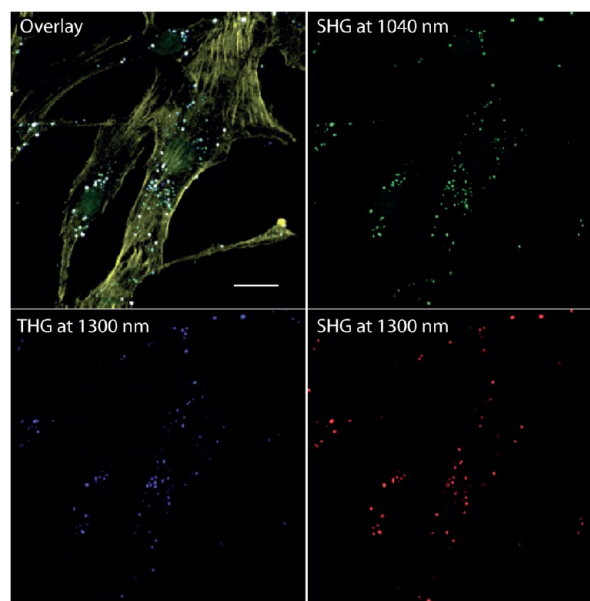

Figure 1. *In vitro* expanded HNP-labeled hMuStem cells. The different panels show the nonlinear responses by HNPs (SHG excited at 1040 and 1300 nm, THG at 1300 nm) and the overlay of these signals with cell bodies, stained in yellow by Phalloidin-Alexa555 (excitation at 1040 nm). Scale bar 20 μm.

vitro expanded hMuStem cells labeled by BFO HNPs to highlight the efficient uptake by the cells of the markers and exemplify the concepts of multi-harmonic detection and emission wavelength tunability enabled by these particles. The sample is imaged using two different excitation wavelengths (1040 and 1300 nm). The different panels represent the overlay and the individual images acquired by three independent channels associated with different spectral ranges. HNPs clearly appear in all channels, with strong emissions both for SHG (at 520 for 1040 nm excitation and 650 for 1300 nm excitation) and for THG (at 433 for 1300 nm). Note that THG can only be detected when excited at wavelengths >1050 nm because signals <350 nm are not transmitted by standard microscope objectives. The particles colocalize spatially with hMuStem cells bodies, stained by Phalloidin-Alexa555 visible in yellow in the overlay image. The possibility to freely tune laser excitation is advantageous for avoiding hindrance by autofluorescence and fluorophores used for staining. More importantly, for tissue measurements, it can be applied for adapting the excitation to the tissue optical properties (scattering, absorption). Furthermore, the simultaneous detection of harmonic emission at different nonlinear orders (SHG, THG) can be beneficial for selectivity. For tissue measurements presented in Figure 2 and 3, we used paraformaldheyde-fixed mice muscle biopsies. At least five pieces of muscle from one animal ($n = 1$) were immersed overnight at 4 °C in a nanoparticle solution. The enhanced
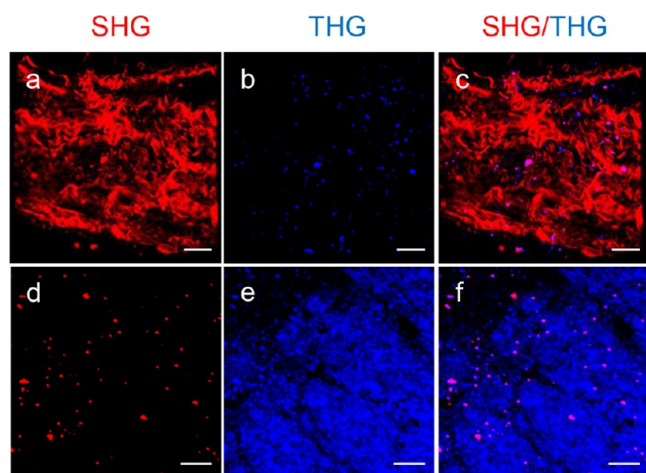
Figure 2. (a−c) Collagen-rich tissue region decorated by HNPs. (a) In the SHG channel, HNPs are not distinguishible from the tissue background. (b) In the THG channel, HNPs appear with no background hindrance. (c) Overlay of SHG and THG channels. (d−f) Spinal chord myelin-rich tissue region decorated by HNPs. (d) In the SHG channel, HNPs are visible with high contrast against background. (e) In the THG channel, HNPs are hindered by the strong background THG. (f) Overlay of SHG and THG channels. Laser excitation 1300 nm. Scale bar 20 μm.
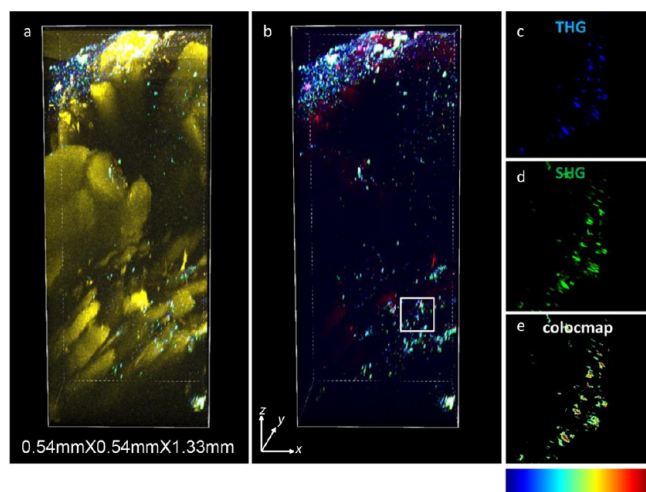

Figure 3. Z-stack of a muscle tissue excited at 1300 nm (THG and SHG) and 1040 nm (autofluorescence). (a) Overlay of all channels. (b) Overlay of SHG and THG channels. (c,d) Maximum intensity projection over the y-axis for the THG and SHG channels of a three-dimensional ROI (0.14 × 0.54 × 0.14 mm³) situated at 0.9 mm from the tissue surface, corresponding to the outlined rectangle in (b). (e) Two-color colocalization image of the ROI in the THG and SHG panels. Hot colors represent positive correlation. The fraction of positively correlated pixels corresponds to I_{corr} = 0.834.[33]

selectivity allowed by HNPs is exemplified in Figure 2a, where we present a muscle tissue characterized by the presence of a collagen fiber network. Such structures are known to generate a strong SHG signal.[22] The presence and position of HNPs in this region can therefore be hardly determined using exclusively information provided by the SHG detection channel. However, one can use the THG channel where HNP emission is acquired without any background disturbance from collagen, as reported in Figure 2b. A similar argument, inversing the role of SHG

with THG, can be applied when HNPs are localized in a fat tissue, as lipid bodies are known to generate strong THG but not SHG.[17] In the experimental conditions described in this article corresponding to administration of cells in skeletal muscle of healthy mice, lipid vesicles are scarcely represented in the tissue composed mostly of muscle fibers and interstitial tissue. In return, dystrophic muscle exhibits a large amount of fat tissue that progressively replaces muscle tissue when muscle precursor cells are exhausted. Nevertheless, the tissue the most described in the literature to be a strong emitter of THG is myelin.[23] It is the reason why we choose to provide image of BFO HNPs in contact with myelin spinal cord in Figure 2d−f. Again, by comparing the SHG and THG channels, we show the ability of this approach to discriminate by harmonic separation the signals generated by HNPs and tissue background.

An additional asset of the approach we propose relies on the extended imaging penetration enabled by NIR-II excitation. On the left side of Figure 3, we present a three-dimensional image-stack of muscle tissue obtained at 1300 nm. The vertical dimension extends for more than 1.3 mm from the sample surface on the top. In the image, one can recognize the intense emission by HNPs as individual or aggregated elements in blue and green over the predominant yellowish autofluorescence by the tissue. Very notably, HNPs can be detected also in the lowest region of the volume at depths exceeding >1 mm. The plots on the right are a split channel representation of the SHG and THG of a region of interest (ROI) embedded in the tissue volume at approximately 1 mm depth. The HNP pattern appears very similar in both detection channels at first sight. For a more quantitative comparison, we computed the colocalization map presented in the bottom plot, where hot colors correspond to high colocalization. Note that the nonuniform color on the large spots in the colocalization map (redder in the center) is a consequence of the fact that the THG image possesses a better spatial resolution, consistently with the decrease of point spread function width as the nonlinear order is increased. This demonstrates that multi-harmonic selective detection can be carried out also in tissue depth, even withstanding the different optical properties of muscles at the SHG and THG wavelengths.

BFO-PEG Cell Labeling Efficiency and Effect on Proliferation. Based on the promising results presented in the previous section, we investigated the effect of exposing to BFO HNPs hMuStem cells isolated from the paravertebralis muscles of patients (n = 3) free of known muscle disease. All details about the procedures for HNPs PEG-coating and in vitro sample preparation are provided in the Materials and Methods section.

Intracellular localization of HNPs is a relevant parameter influencing cell viability but also the scope of the labeling protocol (e.g., nuclear staining vs cytosol or membrane localization). For this reason, we carefully examined the interaction between hMuStem cell organelles and BFO HNPs post-incubation. Our analysis, reported in Figure 4, indicates that at day 4, HNPs are essentially localized in early (labeled by early endosome antigen-1 in yellow, Figure 4a) as well as in late endosomes and lysosomes (stained by Lysotracker in red, Figure 4b). Altogether, these results support an endocytic pathway for HNP internalization going from early to late endosomes and finally lysosomes. Such a situation is very consistent with previous works on PEG-coated BFO HNPs[21] and common to other NPs of similar size, including gold NPs in stem cells.[10]
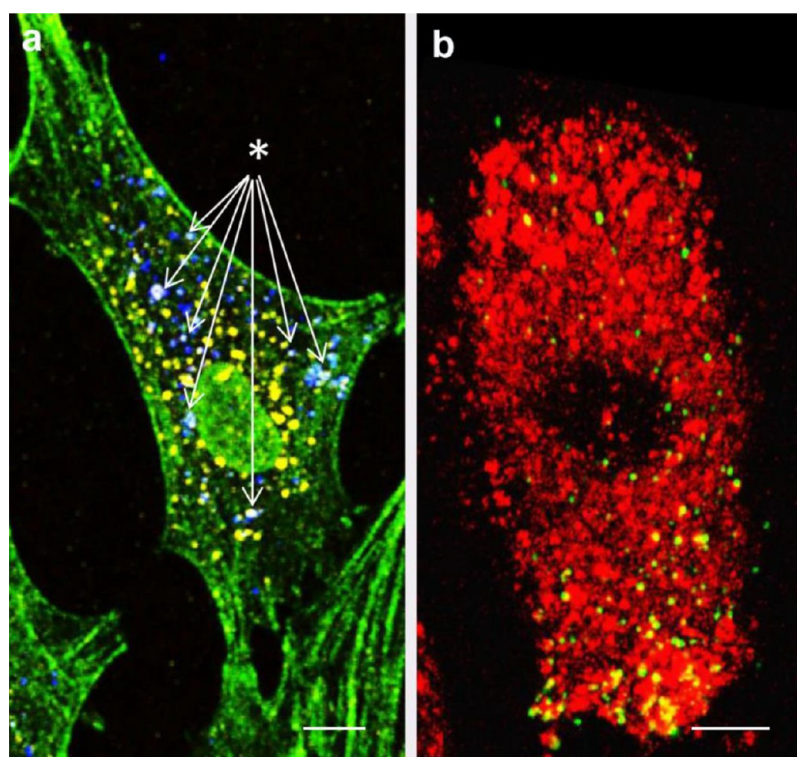
Figure 4. Subcellular PEG-coated BFO HNP localization in cultured hMuStem cells at day 4 post-incubation. (a) Excitation 950 nm. Blue, SHG by HNPs; yellow, fluorescence from EEA1 staining early endosomes; green, Phalloidin-Alexa488 staining cytoskeleton; white, colocalization of HNPs and endosomes. Scale bar 10 μm. (b) Excitation wavelength 1000 nm. Green, SHG by HNPs; red, Lysotracker-Al555 staining lysosomes; yellow, colocalization of red and green signals. Scale bar 10 μm.
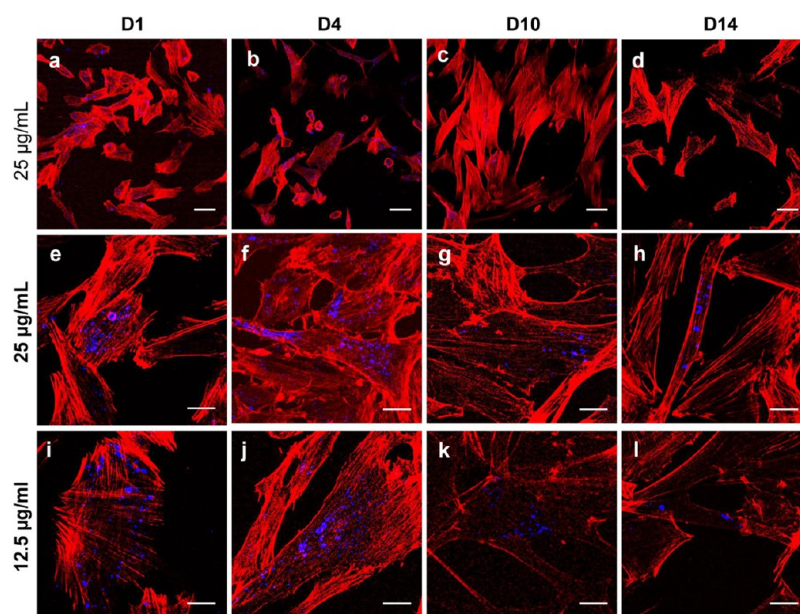

Figure 5. Multiphoton microscopy images of hMuStem cells at different days after exposure to 12.5 and 25 μg/mL PEG-coated BFO HNPs. Blue: SHG by HNPs. Red: actin staining of cell cytoskeleton. Excitation 950 and 1040 nm. Scale bars: (a−d) 100 μm and (e−l) 20 μm.

We then proceeded in the study of the fate of labeled cells over a 2 week period. A series of multiphoton microscopy images of hMuStem cells at different days after labeling are reported in Figure 5. We applied two different HNP concentrations (12.5 and 25 μg/mL) and followed-up the cell cultures until day 14. Qualitatively, we observed that the morphology of hMuStem cells was not impacted by the exposure to HNPs at both concentrations tested. Similarly, we did not retrieve any dead cells, supporting the high viability previously observed for *in vitro* experiments on other human cell lines. Labeling by HNPs is known to be rather sparse, presenting a small average number of SHG spots per cell (typically 10 to 30).[24] These intense spots are associated with

isolated HNPs or more likely to small particle aggregates formed upon uptake and internalization in hMuStem cells.

In Figure 6a, we provide a sequence of histograms reporting the probability for a cell to present a given number of SHG
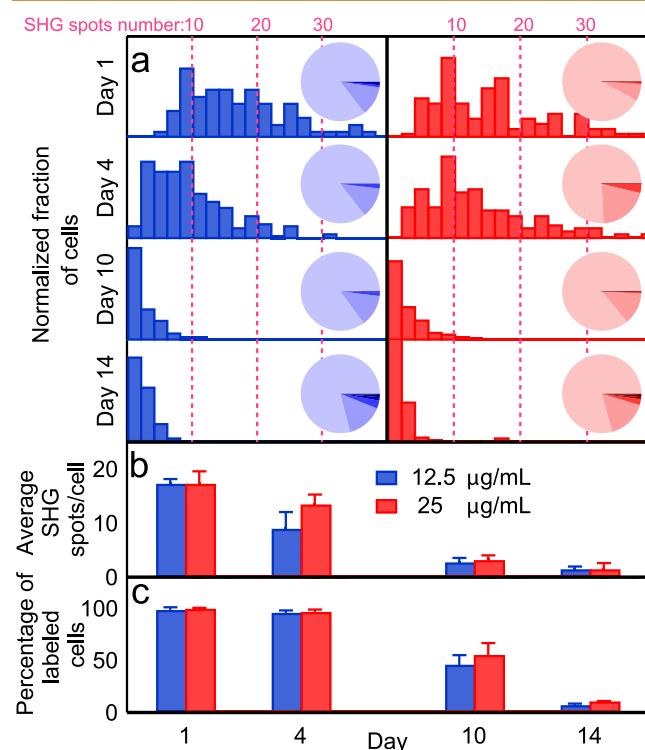

Figure 6. (a) Normalized distributions indicating the fraction of cells with a given number of SHG spots at different days after the exposure protocol (day 0) for the two HNP concentrations tested. The pie charts indicate the distribution of spot sizes at each time point. The lightest color corresponds to 1 pixel (0.46 μm^2) and successive colors to 2, 3, and 4 pixels. (b) Average number of SHG spots per cell. (c) Percentage of HNP-labeled cells according to the definition in the main text. In panels b and c, the error bars indicate the standard deviation calculated for the averages from the three replicates.

spots as a function of day after exposure and particle concentration. The average number of SHG spots per cell is reported in Figure 6b. The procedure applied to determine these values is detailed in the Materials and Methods section. Note that in this case, the error bars are informative of the variability of the three independent replicates from the three donors and not on the width of the probability distributions of Figure 6a. Overall, we note that the labeling does not change significantly until day 4 with rather large particle distributions in cells and no major effect of concentration. For longer times, we observe a major decrease in the number of spots per cell. Such a phenomenon is not surprising, as cells maintained in *in vitro* are known to proliferate very fast and undergo a rapid sequence of doublings with a major impact on labeling. It should be noted that when cells are injected and engrafted, we do not expect a major decrease of cell labeling. Finally, in Figure 6c, we provide the fraction of hMuStem cells labeled over time for the two different BFO HNP concentrations. These values and corresponding error estimates are obtained as the average of the three independent biological replicates. Given the sparse labeling by BFO HNPs, the criterion we selected to describe a labeled cell is that at least one SHG spot is visible on the cell.

The efficiency is determined by dividing the number of cells labeled by the total number of cells (150 to 400 cells by condition). Until day 4, close to the totality of cells were found labeled. Ten days after HNP uptake, 50% of cells are still labeled, whereas at 14 days, this value is reduced to approximately 10%. No significant difference is observed among the two HNP concentrations at any time.

The size of SHG spots for BFO-PEG-labeled cells at both 12.5 and 25 $\mu g/mL$ concentrations was determined from images taken with a 25× objective (pixel size 0.678 μm) at days 1, 4, 10, and 14. The pie charts in Figure 6a indicate the distribution of spot sizes over time. The lightest color corresponds to 1 pixel (0.46 μm^2) and successive colors to groups constituted by 2, 3, and 4 pixels. In all conditions, we observe that more than 80% of the HNP spots have an area equivalent to that of a single pixel. Moreover, we do not report any significant spot size evolution over time for these *in vitro* expanded cells for both HNP concentrations applied.

We successively monitored the effect of HNP exposure on cell viability and proliferation. In Figure 7a, we show the
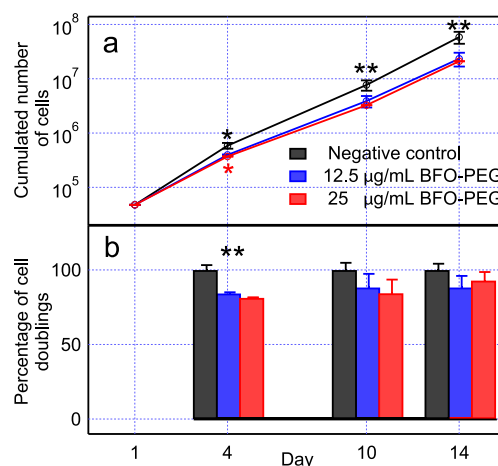

Figure 7. (a) Cumulated number of cells over time for negative control and for the two concentrations tested. (b) Cumulated number of doublings for cells labeled at the two HNP concentrations with respect to negative control, normalized at 100% for every time point. The error bars indicate the standard deviation calculated for the averages from the three patients. HNP labeling procedure at day 0. Significance is calculated by statistical tests: **$p < 0.01$, *$0.01 < p < 0.05$, not significant otherwise. Black * difference of labeled *vs* control; red * difference among the two HNP concentrations.

cumulated number of cells over time for the two HNP concentrations tested (three independent batches per condition) and the negative control. We assessed that there exists a significant difference between the cumulated number of cells in negative control and the labeled cells at both concentrations. However, we also notice that the overall growth trend is similar for the three traces pointing to the absence of major negative impact of the HNPs on the proliferation ability of hMuStem cells. The difference among the two concentrations is significant only at day 4. Similarly, in Figure 7b, we present the cumulated number of cell doublings with respect to negative control, normalized at 100% at each time point. In this case, one can observe only a minor decrease in cell doublings upon HNP labeling at both concentrations at day 4. This difference remains not significant at any other time point.

Tracking BFO-PEG-Labeled hMuStem Cells in Muscle.
To assess the possibility of using HNP-based labeling to track cells of interest in tissue, BFO-PEG hMuStem cells were injected in mice muscle. The experiment was performed on three mice ($n = 3$) to check for reproducibility. As reported in Figure 8, 24 h later, injected tissue was removed and the
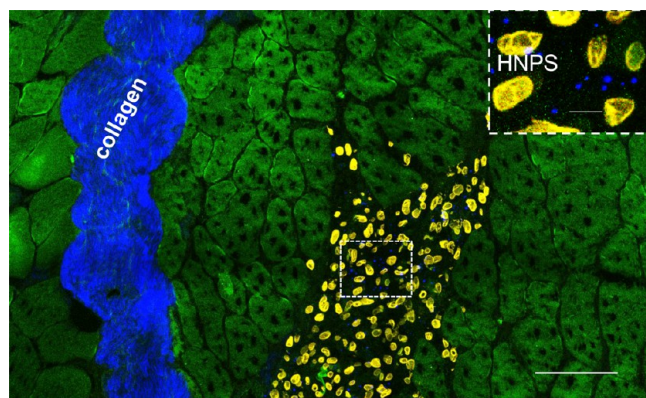

Figure 8. Muscle tissue detection of HNP-labeled hMuStem cells, 24 h post-injection. Blue: SHG from HNPs and collagen. Green: autofluorescence from fiber. Yellow: lamin A/C-Alexa555 immunolabeling for hMuStem cells. Scale bar 100 μm. Inset. Close-up of a ROI in the main image. Excitation at 950 nm. Scale bar 10 μm.

presence of hMuStem cells identified by multiphoton microscopy *ex vivo* in a 25 μm thick slice by specific human lamin A/C immunolabeling and by HNP SHG (in yellow and blue, respectively). hMuStem cells and HNPs are mainly localized in the central region of the image. By inspecting the close-up frame, one can see how the HNPs appear as isolated blue spots in close vicinity of yellow labeled cells. The blue region extending vertically on the left side of the figure corresponds to the intense SHG emission by a bundle of collagen fibers. Although the interpretation of these features is rather clear here because of the distinct morphologies and spatial separation of the different constituents, it is evident that due to the presence of collagen, a straightforward association of SHG with HNPs is not always sufficient for their selective identification.

To ensure that HNPs remain internalized in cells even upon injection in muscle, we took advantage of the abundance of actin filaments for visualizing hMuStem cells by AlexaFluor488-Phalloidin labeling. In this case, as shown in Figure 9, hMuStem cells are identified in tissue by their double immunolabeling lamin A/C (red) and Phalloidin (green). Results again confirm that HNP signals perfectly and exclusively colocalize with the fluorophores staining the cells of interest. Also, this figure is a further demonstration that, thanks to their extremely narrow emission spectra and their excitation tunability, HNPs can be used in association with a large number of fluorophores with no signal cross-talk.

DISCUSSION

In the field of regenerative medicine, tissue homing, survival, differentiation, and engraftment properties of cell candidates need to be clearly understood without artifacts after *in vivo* delivery protocol, in order to objectively assess the therapeutic potential of cell-based strategies developed over the past decade. To this end, the development of noninvasive and powerful imaging technologies is required to overcome the
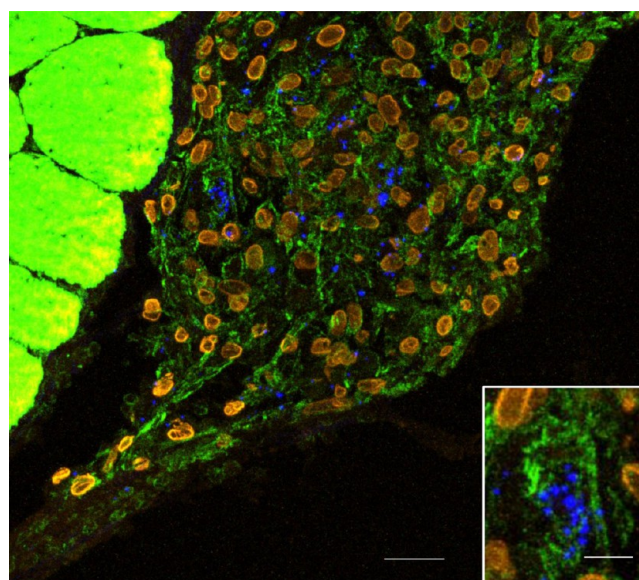

Figure 9. BFO-PEG-labeled hMuStem cell tracking (12.5 μg/mL) in muscle 24 h post-injection. SHG from BFO-PEG, immunolabeling for hMuStem cells: Phalloidin-Alexa488, lamin A/C-Alexa555. Scale bar 25 μm. Inset. Close-up of a ROI in the main image. Excitation at 950 nm. Scale bar 10 μm.

current lack of efficient tools. The outstanding potentialities of multimodal nanomaterials naturally received great attention due to their appealing properties in terms of sensitivity, specificity, and stability enabling long-term follow-up. The high spatial resolution associated with optical techniques and *a fortiori* with nonlinear ones represents a major asset to position them as tool of choice for reliable assessment of advanced therapeutic strategies. However, limited imaging depth and poor signal selectivity in tissues might prevent the use of optical microscopy in relevant preclinical conditions. Here, we show that labeling adult stem cells by HNPs can greatly mitigate these two issues. First, one of the key advantages of this approach relies on the possibility to use NIR-II excitation to minimize the scattering contribution on the excitation path and signal absorption during detection path. In support of this general statement, in our previous works, we numerically computed the imaging depth of HNP retrieval in tissues as a function of NIR excitation wavelength, taking into full account the nonlinear excitation process at the second[25] and third order[15] based on exsisting light transport codes.[26] More recently, Sordillo *et al.* experimentally compared the total attenuation length, l_t, for different tissue types at various excitation wavelengths from 500 to 2500 nm.[12] The optical parameter l_t accounts for both scattering and absorption, and it is the most relevant one for predicting the behavior of the ballistic component of light in a biological medium.[27] Note that this photon fraction is the only one contributing to nonlinear excitation in multiphoton microscopy as it conserves the pulse temporal structure and, therefore, pulse peak intensity, along with propagation. The authors estimated that l_t in NIR-II is 125 μm for muscle, that is, 40% longer than that in NIR-I.[12] On the other hand, the scattering present at the shorter emission wavelengths does not sensibly affect imaging resolution and sensitivity. In a somehow counterintuitive manner, increased scattering for the generated signal can even benefit image quality in epi-detection when a low-magnification, large NA objective is employed.[28] Here, we show that using 1300 nm
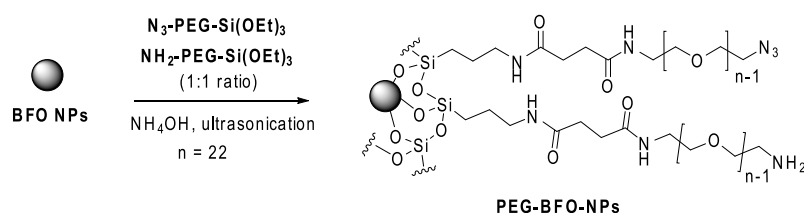
Figure 10. BFO HNP coating procedure.

excitation and a NA 1.1, 25× lens, HNPs embedded at a depth exceeding 1 mm in muscle tissue can be easily detected (Figure 3). Such tissue depth is not yet quite adapted for monitoring cell fate from therapeutic point of view. Nevertheless, it could enable generating *ex vivo* 3D investigation to get major information on the behavior of hMuStem cells in their muscle environment, considering their localization with muscle fibers or the interactions they developed with resident and circulating cells. In addition, it can offer the possibility *in vivo* to track HNP-labeled hMuStem cells and follow them long-term by using intravital microscopy *via* muscle windows. In addition, we have confirmed with the present study that contrast and selectivity can be further boosted by the application of multi-harmonic HNP detection that results in the particularly important presence of strong autofluorescence or collagen/lipid harmonic emission, as exemplified in Figures 2 and 8.[15] HNPs are not prone to bleaching or blinking because of their nonparametric interaction with the excitation field, which does not imply absorption and re-emission.[14,19] Such a property is essential to perform tracking over days or weeks. Finally, HNP excitation wavelength flexibility widens the palette of molecular probes that can be used for fluorescence staining of the structures of interest, as their narrow emission peaks can always be spectrally isolated by simply tuning the laser wavelength outside the fluorophores' absorption region. Clearly, all these advantages would vanish if the interaction of HNPs with cells would affect viability and proliferation. This motivated the thorough bioassessment presented in this work, where we show that PEG-coated BFO HNPs in contact with hMuStem cells allow long-term monitoring with no impact on their essential features as compared to negative controls. Despite some small discrepancies, the two particle concentrations applied seem to differ on cell proliferation and labeling efficiency in a very limited fashion. We are tempted to ascribe this observation together with the minor impact of HNPs on cells to the active uptake of particles by cells and their successive storage in endosomes and lysosomes, which might limit the negative effect of internalized nano-objects on cellular metabolisms. In terms of labeling efficiency and stability over time, we demonstrated that by applying our protocol almost the totality of cells are marked up to day 4, despite a substantial increase in the number of cumulated cells from day 1 to day 4. At later times, the decrease in labeling that we observe can be ascribed to the continuous proliferation activity of cells peculiar to *in vitro* cultures[3,29] and should therefore not prevent the long-term observation of HNP-labeled hMuStem cells injected in muscles. Note that protocols for monitoring cell dissemination after systemic delivery prescribe follow-up of the fate of injected cells typically for 72 h.

CONCLUSIONS

PEG-coated BFO HNPs in association with NIR-II multi-photon microscopy represent an innovative research platform for assessing cell therapies at high spatial resolution. Here, we demonstrate this procedure by labeling hMuStem cells, a human skeletal muscle-derived stem cell population with promising therapeutic potential for muscular dystrophies. During a 14 day monitoring period, we observe *in vitro* very limited adverse effects on cell survival as well morphological and proliferation features. Cell labeling is highly stable as highlighted by the observation that 98% of cells are labeled at 4 days post-incubation. By immunolabeling and image signal colocalization, we evidence that BFO HNPs preferentially follow an endocytic internalization pathway. Successively, we show the possibility to retrieve hMuStem cells in mice muscles up to 24 h post-injection. BFO-PEG is able to generate intense SHG and THG simultaneously. Such a multi-harmonic emission is essential to distinguish particles from the SHG generated by collagen and THG by lipids in muscles. In terms of signal intensity, we demonstrated the possibility to retrieve them at depths exceeding 1 mm in muscle. Our results show that the labeling of hMuStem cells with BFO-PEG represents a promising approach for monitoring their engraftment properties.

MATERIALS AND METHODS

Human Muscle Tissue. Muscle samples were obtained from paravertebralis muscles of 12−15 year old patients free of known
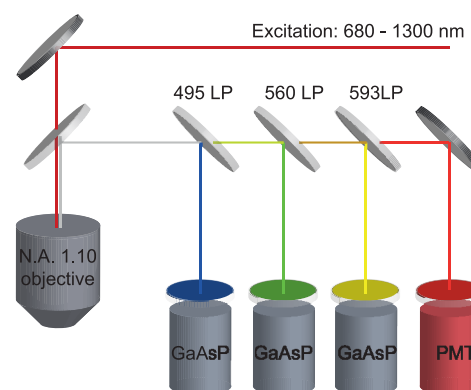

Figure 11. Definition of the channels in the nondescanned detection unit. LP: long-pass dichroic mirror. GaAsP: gallium arsenide phosphide detector. PMT: photomultiplier.

muscle disease and operated for acute scoliosis at the Department of Pediatric Surgery of the Centre Hospitalier Universitaire (CHU) de Nantes (France). All patients gave written informed consent. All protocols were approved by the Clinical Research Department of the CHU (Nantes, France), according to the rules of the French Regulatory Health Authorities. Biological sample bank was done in compliance with the national guidelines regarding the use of human tissue for research (Permit numbers: MESR/DC-2010-1199; CPP/29/10).

Table 1. Settings Used for All the Images Presented[a]

Figure	exc (nm)	blue	green	yellow	red
2	1240	THG (415/10)			SHG (615/20)
3	1300/1040	THG (446/92)	SHG (525/50)	Autofluo (575/25)	SHG+Autofluo (629/56)
4a	950	SHG (446/92)	Phalloidin-Alexa488 (525/50)	EEA1-Alexa555 (575/25)	
4b	950/1040		SHG (525/50)		Lysotracker Alexa568 (629/56)
5	950/1040	SHG (446/92)		Phalloidin-Alexa555 (525/50)	
8, 9	950	SHG (446/92)	Phalloidin-Alexa488 (525/50)	Lamin a/c Alexa555 (575/25)	

[a]Blue, green, yellow, and red columns correspond to the different non-descanned detection channels defined in Figure 11 used for detecting the fluorescence and harmonic signals. The specifications of the spectral filters used for each image are provided in brackets as (central wavelength/bandwidth). Double excitation (e.g., 950/1040) indicates the use of both tunable and fixed wavelength output of the laser for image acquisition.

Muscle-derived cells (MDCs) were isolated after 6 days using a modified version of the preplating technique previously described.[3] They were plated at 5×10^3 viable cells/cm^2 to gelatin-coated plastic flasks (Corning) under standard conditions (37 °C in 95% humidified air and 5% CO$_2$) and amplified in growth medium (Macopharma, Mouvaux, France) containing 10% FCS, 1% PSF/10 ng/mL human recombinant basic fibroblast growth factor, and 25 ng/mL human recombinant epidermal growth factor (Miltenyi).

Animals. 129/J mice were housed in the specific pathogen-free animal facility at Oniris (Nantes, France). Mice were fed ad libitum and allowed continuous access to tap water. Three-month-old mice were used as recipients for human cell implantation. All surgeries were performed under ketamine/xylazine anesthesia. All experiments were carried out in accordance with the guidelines from the French National Research Council for the Care and Use of Laboratory Animals (reference number: APAFIS #1267-2015072317573209).

Nanoparticle Preparation and Characterization. The coating procedure was adapted from previously reported protocol.[21,30] Heterobifunctional PEG oligomers were prepared according to established synthetic protocols.[31] As reported in Figure 10, a mixture of EtOH/toluene (1:1, 2.38 mL) and aqueous ammonia (25%, 762 μL) was added to a suspension of BFO NPs (in EtOH, 3.6 mg/mL, 5 mg). The suspension was ultrasonicated for 30 min, and a mixture of α-triethoxysilyl-ω-azido PEG and α-triethoxysilyl-ω-amino PEG (1:1, 150 mg) was added. After ultrasonication at 40 °C for 12 h, the suspension was concentrated to 0.5 mL. Emulsification in a mixture of CH$_2$Cl$_2$/EtOH/H$_2$O (1:1:1, 3 mL), followed by centrifugation (10 min, 13 000 rpm), was repeated five times to remove the excess of unreacted polymers in the aqueous layer and to collect the suspension of PEG-BFO NPs in CH$_2$Cl$_2$. The solvent was removed in vacuo, and PEG-BFO NPs were suspended in EtOH.

Concentration was calculated by measuring the turbidity of the solution by spectrometry at 600 nm (Synergy HT) and by comparing the values with a standard curve prepared using the stock solution at 3.6 mg/mL. PEG-BFO NPs were suspended at 4.2 mg/mL and characterized by dynamic light scattering (DLS) using a Zetasizer NanoZ (Malvern) for determination of mean hydrodynamic volume and ζ-potential. Suspension of uncoated or PEG-BFO NPs (20 μL) was diluted in 1 mL of distilled water. Acetic acid (100 μL) was added, and the resulting suspension was ultrasonicated for 30 min and analyzed by DLS. We determined a mean hydrodynamic diameter of 80.10 ± 18.39 nm and ζ-potential = 0.83 ± 0.13 mV.

hMuStem Cell Labeling by BFO-PEG HNPs. hMuStem cells were expanded for 8 h in a plastic flask. Successively, they were exposed to BFO-PEG HNPs at 12.5 and 25 μg/mL overnight at 37 °C. Culture medium was removed, and primary cell cultures were maintained for 14 days. Cells were washed in phosphate-buffered saline solution (PBS) at pH 7.4 and fixed in 4% paraformaldehyde at T_0, $T_0 + 1d$, $T_0 + 4d$, $T_0 + 10d$, and $T_0 + 14d$.

In Vitro Proliferation Analysis. Labeled hMuStem cells ($n = 3$, independent batch) were plated in a gelatin-coated flask at a density of 5×10^4 cells/cm^2 in growth medium and placed under standard conditions. Cell population growth was monitored over a period of 14 days. The population doubling level was calculated at each passage performed when cultures reached 80% confluence, as previously described.[32] The number of spots per cell was determined by using the

Find maxima algorithm of ImageJ 1.51h (Fiji Distribution) public domain software to segment locally bright structures. Area values of spots were determined by using the function Adjust threshold and Analyze particles. By this dual operation, we retrieved information about the number of spots in the cells and the distribution of their size for each HNP concentration and each in vitro expansion time considered.

Statistical analysis was performed using the Statistics and Machine Learning Toolbox of the software MATLAB R2015b. We applied both Student t test sequentially on each labeled sample against the negative control and one-way ANOVA on the two samples labeled at different concentrations and negative control simultaneously.

In Vivo Experiment and Histological Analysis. Mice ($n = 3$) were anesthetized with an intraperitoneal injection (0.1 mL per 20 g body weight) of a solution containing 100 mg/mL ketamine (Merial, Lyon, France) and 20 mg/mL Rompun 2% (Bayer, Puteaux, France) in NaCl solution. Labeled hMuStem cells were trypsinized, pelleted, resuspended (2.5×10^5 cells in 15 μL of PBS), and injected through the skin into left Tibialis anterior (TA) muscle, using a 50 μL syringe with a 29-gauge needle. Twenty-four hours later, injected muscles were removed, frozen in isopentane/liquid nitrogen, and cryosectioned at 10 μm. Transverse muscle sections were disposed on a slide and submitted to immunolabeling. Nuclei of hMuStem cells were detected using specific human lamin A/C antibody combined to AlexaFluor555-conjugated secondary antibody. Actin was detected with Phalloidin-AlexaFluor488.

Multiphoton Imaging. Measurements were performed at the APEX platform of the INRA/Oniris UMR 703 (Nantes, France). A Nikon microscope A1R-MP coupled with a Insight Deepsee laser (Spectra Physics), tunable in the 680−1300 nm range, <120 fs pulse width was used. An auxiliary beam at 1040 nm can be used in combination with the tunable output for dual wavelength excitation. Auto laser alignment was systematically performed when changing multiphoton excitation wavelength. For all images, an apochromat 25× MP1300 immersion objective (NA 1.10, WD 2.0 mm) was employed. As reported in Figure 11, the microscope non-descanned detector unit was equipped with three highly sensitive GaAsP on the blue, green, and yellow channels and a photomultiplier tube on the red channel. We used different interferometric filters according to the excitation as reported in Table 1. For all images presented, we use color assignments as close as possible to actual colors for all detection channels. For instance, SHG by HNPs excited at 1040 nm (i.e., emitted signal at 520 nm) is represented in green, whereas SHG excited at 1300 nm (650 nm) is in red. Colocalization signals, derived from the spatial superposition of different harmonics by HNPs or of fluorescent markers, will simply appear as the additive mixing of their respective colors.

Colocalization of Harmonic Signal from BFO-PEG in Deep Tissue. We used a plugin for the image processing software ImageJ based on the method originally described by Jaskolski et al.[33] This algorithm computes correlation of intensities between pairs of individual pixels in two different channels. Results are presented as a colocalization color map where hot colors represent positive correlation (colocalization), and colors that are cold represent negative correlation (exclusion).

AUTHOR INFORMATION

Corresponding Author

*E-mail: luigi.bonacina@unige.ch.

ORCID

Sandrine Gerber-Lemaire: 0000-0002-6519-2782

Luigi Bonacina: 0000-0003-0476-4473

Notes

The authors declare no competing financial interest.

REFERENCES

(1) Emery, A. E. Population Frequencies of Inherited Neuromuscular Diseases-a World Survey. *Neuromuscular disord.* 1991, 1, 19−29.

(2) Moat, S. J.; Bradley, D. M.; Salmon, R.; Clarke, A.; Hartley, L. Newborn Bloodspot Screening for Duchenne Muscular Dystrophy: 21 Years Experience in Wales (UK). *Eur. J. Hum. Genet.* 2013, 21, 1049−1053.

(3) Rouger, K.; Larcher, T.; Dubreil, L.; Deschamps, J.-Y.; le Guiner, C.; Jouvion, G.; Delorme, B.; Lieubeau, B.; Carlus, M.; Fornasari, B.; et al. Systemic Delivery of Allogenic Muscle Stem Cells Induces Long-Term Muscle Repair and Clinical Efficacy in Duchenne Muscular Dystrophy Dogs. *Am. J. Pathol.* 2011, 179, 2501−2518.

(4) Robriquet, F.; Lardenois, A.; Babarit, C.; Larcher, T.; Dubreil, L.; Leroux, I.; Zuber, C.; Ledevin, M.; Deschamps, J.-Y.; Fromes, Y.; et al. Differential Gene Expression Profiling of Dystrophic Dog Muscle after MuStem Cell Transplantation. *PLoS One* 2015, 10, e0123336.

(5) Robriquet, F.; Babarit, C.; Larcher, T.; Dubreil, L.; Ledevin, M.; Goubin, H.; Rouger, K.; Guével, L. Identification in GRMD Dog Muscle of Critical miRNAs Involved in Pathophysiology and Effects Associated with MuStem Cell Transplantation. *BMC Musculoskeletal Disord.* 2016, 17, 1.

(6) Lardenois, A.; Jagot, S.; Lagarrigue, M.; Guével, B.; Ledevin, M.; Larcher, T.; Dubreil, L.; Pineau, C.; Rouger, K.; Guével, L. Quantitative Proteome Profiling of Dystrophic Dog Skeletal Muscle Reveals a Stabilized Muscular Architecture and Protection against Oxidative Stress after Systemic Delivery of MuStem Cells. *Proteomics* 2016, 16, 2028−2042.

(7) Chérel, Y.; Rouger, K. MuStem Cells: a Therapeutic Candidate for Cell-Based Therapy of Duchenne Muscular Dystrophy. *Hum. Gene Ther.* 2013, 24, A16−A16.

(8) Rouger, K.; Chérel, Y. Isolation Method of Stem Cells and Their Use in Cell Therapy. Patent Appl. US61/659,538, 2012.

(9) Wu, T.-J.; Tzeng, Y.-K.; Chang, W.-W.; Cheng, C.-A.; Kuo, Y.; Chien, C.-H.; Chang, H.-C.; Yu, J. Tracking the Engraftment and Regenerative Capabilities of Transplanted Lung Stem Cells Using Fluorescent Nanodiamonds. *Nat. Nanotechnol.* 2013, 8, 682−689.

(10) Comenge, J.; Fragueiro, O.; Sharkey, J.; Taylor, A.; Held, M.; Burton, N. C.; Park, B. K.; Wilm, B.; Murray, P.; Brust, M.; et al. Preventing Plasmon Coupling between Gold Nanorods Improves the Sensitivity of Photoacoustic Detection of Labeled Stem Cells in Vivo. *ACS Nano* 2016, 10, 7106−7116.

(11) Xu, C.; Mu, L.; Roes, I.; Miranda-Nieves, D.; Nahrendorf, M.; Ankrum, J. A.; Zhao, W.; Karp, J. M. Nanoparticle-Based Monitoring of Cell Therapy. *Nanotechnology* 2011, 22, 494001.

(12) Sordillo, L. A.; Pu, Y.; Pratavieira, S.; Budansky, Y.; Alfano, R. R. Deep Optical Imaging of Tissue Using the Second and Third Near-Infrared Spectral Windows. *J. Biomed. Opt.* 2014, 19, 056004−056004.

(13) Liu, T.-M.; Conde, J.; Lipinski, T.; Bednarkiewicz, A.; Huang, C.-C. Revisiting the Classification of NIR-Absorbing/Emitting Nanomaterials for in Vivo Bioapplications. *NPG Asia Mater.* 2016, 8, e295.

(14) Bonacina, L. Nonlinear Nanomedecine: Harmonic Nanoparticles toward Targeted Diagnosis and Therapy. *Mol. Pharmaceutics* 2013, 10, 783−792.

(15) Rogov, A.; Irondelle, M.; Ramos Gomes, F.; Bode, J.; Staedler, D.; Passemard, S.; Courvoisier, S.; Yamamoto, Y.; Waharte, F.; Ciepielewski, D.; Rideau, Ph.; Gerber-Lemaire, S.; Alves, F.; Salamero, J.; Bonacina, L.; Wolf, J.-P. Simultaneous Multiharmonic Imaging of Nanoparticles in Tissues for Increased Selectivity. *ACS Photonics* 2015, 2, 1416−1422.

(16) Zipfel, W. R.; Williams, R. M.; Christie, R.; Nikitin, A. Y.; Hyman, B. T.; Webb, W. W. Live Tissue Intrinsic Emission Microscopy Using Multiphoton-Excited Native Fluorescence and Second Harmonic Generation. *Proc. Natl. Acad. Sci. U. S. A.* 2003, 100, 7075−7080.

(17) Débarre, D.; Supatto, W.; Pena, A.-M.; Fabre, A.; Tordjmann, T.; Combettes, L.; Schanne-Klein, M.-C.; Beaurepaire, E. Imaging Lipid Bodies in Cells and Tissues Using Third-Harmonic Generation Microscopy. *Nat. Methods* 2006, 3, 47−53.

(18) Schwung, S.; Rogov, A.; Clarke, G.; Joulaud, C.; Magouroux, T.; Staedler, D.; Passemard, S.; Justel, T.; Badie, L.; Galez, C.; et al. Nonlinear Optical and Magnetic Properties of BiFeO3 Harmonic Nanoparticles. *J. Appl. Phys.* 2014, 116, 114306.

(19) Staedler, D.; Magouroux, T.; Hadji, R.; Joulaud, C.; Extermann, J.; Schwung, S.; Passemard, S.; Kasparian, C.; Clarke, G.; Gerrmann, M.; Le Dantec, R.; Mugnier, Y.; Rytz, D.; Ciepielewski, D.; Galez, C.; Gerber-Lemaire, S.; Juillerat-Jeanneret, L.; Bonacina, L.; Wolf, J.-P. Harmonic Nanocrystals for Biolabeling: A Survey of Optical Properties and Biocompatibility. *ACS Nano* 2012, 6, 2542−2549.

(20) Schmidt, C.; Riporto, J.; Uldry, A.; Rogov, A.; Mugnier, Y.; Le Dantec, R.; Wolf, J.-P.; Bonacina, L. Multi-Order Investigation of the Nonlinear Susceptibility Tensors of Individual Nanoparticles. *Sci. Rep.* 2016, 6, 25415.

(21) Staedler, D.; Passemard, S.; Magouroux, T.; Rogov, A.; Maguire, C. M.; Mohamed, B. M.; Schwung, S.; Rytz, D.; Jüstel, T.; Hwu, S.; Mugnier, Y.; le Dantec, R.; Volkov, Y.; Gerber-Lemaire, S.; Prina-Mello, A.; Bonacina, L.; Wolf, J.-P. Cellular Uptake and Biocompatibility of Bismuth Ferrite Harmonic Advanced Nanoparticles. *Nanomedicine* 2015, 11, 815−828.

(22) Williams, R. M.; Zipfel, W. R.; Webb, W. W. Interpreting Second-Harmonic Generation Images of Collagen I Fibrils. *Biophys. J.* 2005, 88, 1377−1386.

(23) Farrar, M. J.; Wise, F. W.; Fetcho, J. R.; Schaffer, C. B. *In Vivo* Imaging of Myelin in the Vertebrate Central Nervous System Using Third Harmonic Generation Microscopy. *Biophys. J.* 2011, 100, 1362−1371.

(24) Magouroux, T.; Extermann, J.; Hoffmann, P.; Mugnier, Y.; le Dantec, R.; Jaconi, M. E.; Kasparian, C.; Ciepielewski, D.; Bonacina, L.; Wolf, J.-P. High-Speed Tracking of Murine Cardiac Stem Cells by Harmonic Nanodoublers. *Small* 2012, 8, 2752−2756.

(25) Extermann, J.; Bonacina, L.; Cuna, E.; Kasparian, C.; Mugnier, Y.; Feurer, T.; Wolf, J. P. Nanodoublers as Deep Imaging Markers for Multi-Photon Microscopy. *Opt. Express* 2009, 17, 15342−15349.

(26) Wang, L.; Jacques, S. L.; Zheng, L. MCML Monte Carlo Modeling of Light Transport in Multi-Layered Tissues. *Comput. Methods Programs Biomed.* **1995**, *47*, 131−146.

(27) Yoo, K.; Alfano, R. Time-Resolved Coherent and Incoherent Components of Forward Light Scattering in Random Media. *Opt. Lett.* **1990**, *15*, 320−322.

(28) Débarre, D.; Olivier, N.; Beaurepaire, E. Signal Epidetection in Third-Harmonic Generation Microscopy of Turbid Media. *Opt. Express* **2007**, *15*, 8913−8924.

(29) Wang, Y.; Zhou, X.; Chen, Z.; Cai, B.; Ye, Z.; Gao, C.; Huang, J. Synthesis of Cubic LiNbO$_3$ Nanoparticles and Their Application *in Vitro* Bioimaging. *Appl. Phys. A: Mater. Sci. Process.* **2014**, *117*, 2121−2126.

(30) Passemard, S.; Staedler, D.; Sonego, G.; Magouroux, T.; Schneiter, G. S.; Juillerat-Jeanneret, L.; Bonacina, L.; Gerber-Lemaire, S. Functionalized Bismuth Ferrite Harmonic Nanoparticles for Cancer Cells Labeling and Imaging. *J. Nanopart. Res.* **2015**, *17*, 1−13.

(31) Passemard, S.; Staedler, D.; Ucnova, L.; Schneiter, G. S.; Kong, P.; Bonacina, L.; Juillerat-Jeanneret, L.; Gerber-Lemaire, S. Convenient Synthesis of Heterobifunctional Poly (Ethylene Glycol) Suitable for the Functionalization of Iron Oxide Nanoparticles for Biomedical Applications. *Bioorg. Med. Chem. Lett.* **2013**, *23*, 5006−5010.

(32) Blasco, M. A.; Lee, H.-W.; Hande, M. P.; Samper, E.; Lansdorp, P. M.; DePinho, R. A.; Greider, C. W. Telomere Shortening and Tumor Formation by Mouse Cells Lacking Telomerase RNA. *Cell* **1997**, *91*, 25−34.

(33) Jaskolski, F.; Mulle, C.; Manzoni, O. J. An Automated Method to Quantify and Visualize Colocalized Fluorescent Signals. *J. Neurosci. Methods* **2005**, *146*, 42−49.